Loss and Deviation in Windmilling Fans

Ewan J. Gunn
Whittle Laboratory, University of Cambridge
1 JJ Thomson Avenue, Cambridge CB3 0DY, UK
ejg55@cam.ac.uk
ASME Student Member

Cesare A. Hall[1]
Whittle Laboratory, University of Cambridge
1 JJ Thomson Avenue, Cambridge CB3 0DY, UK
cah1003@cam.ac.uk
ASME Member

ABSTRACT

For an unpowered turbofan in flight the airflow through the engine causes the fan to freewheel. This paper considers the flow-field through a fan operating in this mode, with emphasis on the effects of blade row losses and deviation. A control volume analysis is used to show that windmilling fans operate at a fixed flow coefficient which depends on the blade metal and deviation angles, while the blade row losses are shown to determine the fan mass flow rate. Experimental and numerical results are used to understand how the loss and deviation differ from the design condition due to the flow physics encountered at windmill. Results are presented from an experimental study of a windmilling low-speed rig fan, including detailed area traverses downstream of the rotor and stator. 3D CFD calculations of the fan rig and a representative transonic fan windmilling at a cruise flight condition have also been completed. The rig test results confirm that in the windmilling condition the flow through the fan stator separates from the pressure surface over most of the span. This generates high loss and the resulting blockage changes the rotor work profile leading to modified rotational speed. In the engine fan rotor, a vortex forms at the pressure surface near the tip and further loss results from a hub separation caused by blockage from the downstream core and splitter.

INTRODUCTION

Aircraft operability at an engine-out condition is strongly influenced by the aerodynamic performance of the fan stage. At this condition the combustor is unlit, the engine produces no power and the fan freewheels due to the ram pressure of the oncoming air. This is defined as the windmill operating point. It is important to know the resulting drag force on the engine since this influences the size of the aircraft vertical stabiliser. The fan rotational speed is also critical as this determines the magnitude and frequency of vibrational loads passed to the aircraft as well as the shaft bearing requirements. This paper is concerned with the turbomachinery aerodynamics of the windmilling fan stage, and in particular the distribution of blade row losses and flow angles and their influence on the engine drag and shaft speed.

Previous studies have shown that windmilling fans operate with high loss due to negative incidence onto both the rotor and stator vanes. Prasad and Lord (2010) presented results from a full-scale engine test at windmill. They found that the majority of loss occurred in the stator vane, which operates at negative incidence due to the substantially axial flow exiting the rotor. Similarly, García Rosa et al (2012), using experiments conducted in a turbofan test rig, showed that the fan outlet

[1] Corresponding author

guide vane operates under severe off-design incidence leading to major flow separation. In other cases, such as Gill et al (2010) or Goto et al (2014), severe flow separations were predicted in the stator, although the rotor was also found to operate at high levels of loss with local separations.

The relative flow angle at rotor exit determines the local work input to the flow and therefore where the fan operates as a compressor and where it operates as a turbine. Prasad and Lord (2010) found that the relative flow left the rotor at nearly the blade angle. Goto et al (2014) also show windmill results with small rotor deviation angles. In both these cases, the rotor flow appears to be reasonably attached. In cases where parts of the rotor show larger separations, such as in Courty-Audren (2010) or Gill et al (2010), the deviation appears to be greater, although the values are not explicitly stated. It is worth noting that in García Rosa et al. (2012) and Goto et al (2014), the bottom 50% of the rotor span operates as a compressor and the top 50% as a turbine. In contrast, in Prasad and Lord (2010), the cross-over point between turbine and compressor is around 60% span.

Figure 1 is a sketch of the velocity triangles for a section through a fan stage operating at design and windmill conditions. The velocity vectors have been scaled such that the axial velocities for the two conditions are shown as the same. This sketch indicates that the fan flow coefficient (V_x/U) is increased relative to design leading to negative incidence onto the rotor. At exit from the rotor, the low blade speed leads to low absolute swirl velocity and highly negative incidence onto the stator, which can be expected to separate on the pressure surface, as shown in previous work. For this particular case, the rotor section is shown with significant deviation and negative absolute swirl at rotor exit. It is therefore operating as a "turbine". The velocity triangles show that as deviation and relative swirl angle β_3 increases, the rotor section will tend to operate more like a turbine and thus extract more work from the flow or cause the rotor speed to increase.

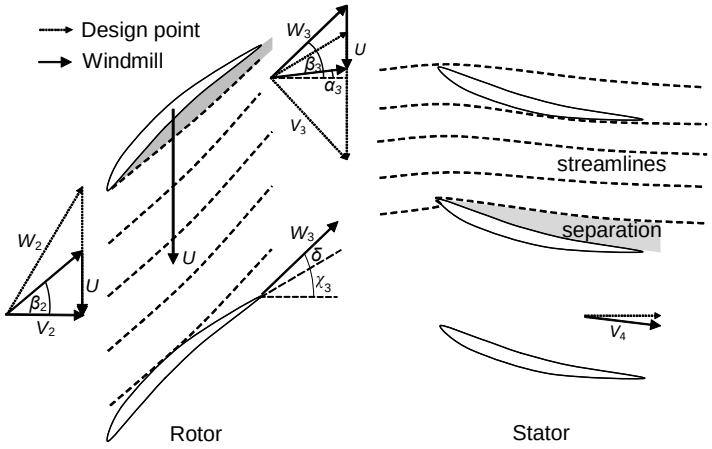

Figure 1: Velocity triangles for a windmilling fan section.

This paper sets out to improve our understanding of the sources and effects of loss and deviation within a windmilling fan. In particular, it aims to show how loss and deviation affect windmilling engine mass flow, rotational speed and drag. It also aims to present the detailed mechanisms responsible for generating loss and deviation in a windmilling fan and to show what aerodynamic differences there are between a low-speed fan and a transonic fan stage.

The approach taken is firstly to use simple compressible relations and the fundamental laws to reveal the broad trends of how fan rotational speed and mass flow vary with flight Mach number, blade row losses and rotor exit flow angle. Two test cases are then presented: one a low-speed fan rig and the other a transonic fan geometry typical of a high bypass ratio turbofan. The low-speed rig has been run at windmill and flow traverses have been completed at exit from the rotor and stator. This case has also been computed in unsteady CFD. The results are used to understand the fan flow field, with particular focus on the losses and distribution of work. The transonic fan has been run at windmill using the same CFD methodology and the differences from the low speed case are examined. The detailed flow field around the rotor pressure surface and through the bypass system are also presented to further understand the loss sources present.

CONTROL VOLUME ANALYSIS

Figure 2 is a sketch of the capture streamtube for a windmilling turbofan extending from far upstream to far downstream. The engine is unlit and Prasad and Lord (2010) showed that under windmilling conditions the shaft power can be neglected, as the fan stage loading value was found to be two orders of magnitude smaller than the value at a ground idle condition. This streamtube can be therefore be considered as a control volume for which there is zero heat or work exchange, but with a change in axial momentum leading to a drag force on the engine, F_D. In this section, conservation of mass, momentum and energy are applied to the engine streamtube to explore the expected variations in windmilling performance with stagnation pressure losses and rotor exit flow angle.

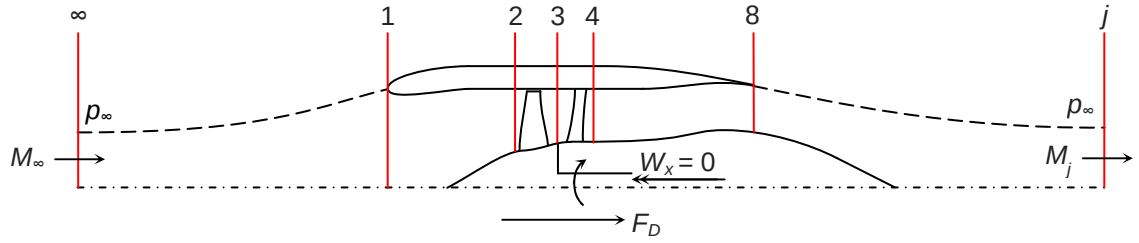

Figure 2: Capture streamtube used as the control volume for a windmilling turbofan.

Conservation of Mass

The following definition of engine non-dimensional mass flow is used, which is a function of Mach number at fan inlet only:

$$\tilde{\dot{m}}_2 = \frac{\dot{m}\sqrt{c_p T_{02}}}{A_2 p_{02}} = Q\left(M_2\right) \tag{1}$$

Since there is no work input, $T_{08} = T_{02}$, the non-dimensional mass flow can be written as:

$$\tilde{\dot{m}}_2 = \frac{\dot{m}\sqrt{c_p T_{0j}}}{A_j p_{0j}} \frac{p_{0j}}{p_{02}} \frac{A_j}{A_2} \cong Q\left(M_j\right) \frac{p_{08}}{p_{01}} \frac{A_8}{A_2} \tag{2}$$

The above equation assumes there is negligible loss upstream of the fan and downstream of the engine, $p_{01} = p_{02}$ and $p_{08} = p_{0j}$. Any flow through the core is neglected as this will be small for a high bypass ratio turbofan, see Walsh and Fletcher (1998). In addition, the jet area is approximated to be equal to the exit nozzle area $A_8 = A_j$. This should be reasonably valid, since at windmill, the exit nozzle is unchoked and the static pressure at the nozzle exit plane will be close to ambient, see Cumpsty and Heyes (2015). Given that the inlet and exit are at the same static pressure, the jet Mach number can be found using:

$$M_j^2 = \left\{ \left(\frac{p_{08}}{p_{01}} \right)^{(\gamma-1)/\gamma} \left(1 + \frac{\gamma-1}{2} M_\infty^2 \right) - 1 \right\} \frac{2}{\gamma-1} \tag{3}$$

The non-dimensional mass flow given in eqn. (2) is therefore fixed by the flight Mach number, M_∞, the fan-face to nozzle area ratio A_2/A_8, and any change in stagnation pressure through the streamtube, p_{08}/p_{01}.

Euler Work Equation

The Euler work equation can be applied to the fan rotor at an average radius with zero work input and zero inlet swirl (consider the velocity triangles in Fig. 1 with $\alpha_3 = 0$):

$$\Delta h_0 = \bar{U}\left(V_{\theta 3}\right) = \bar{U}\left(V_{x3} \tan \beta_3 - \bar{U}\right) = 0 \tag{4}$$

The fan flow coefficient at windmill can then be written as:

$$\phi = \frac{\dot{m}}{\rho_2 A_2 \bar{U}} = \frac{V_{x2}}{\bar{U}} = \frac{V_{x2}}{V_{x3}} \cot\left(\chi_3 + \delta\right) \tag{5}$$

The flow coefficient therefore depends on the rotor deviation. The non-dimensional speed can be written in terms of the non-dimensional mass flow and flow coefficient, using eqns. (1) and (5):

$$\tilde{U} = \frac{\bar{U}}{\sqrt{c_p T_{01}}} = \frac{\tilde{\dot{m}}_2}{\phi} \frac{\rho_{02}}{\rho_2} \frac{\gamma - 1}{\gamma} \tag{6}$$

Streamtube losses

The streamtube losses are made up of the installation duct losses, the fan rotor losses and the stator losses. Assuming a total pressure recovery of the installation of 0.98, based on the results of Prasad and Lord (2010) at low flow rates, and using mean stagnation pressure loss coefficients for the blade rows at a single average radius, the ratio of engine exit to inlet stagnation pressure can be written as:

$$p_{08}/p_{01} \cong 0.98 - Y_{p,R}\left(1 - p_2/p_{02,rel}\right) - Y_{p,S}\left(1 - p_3/p_{03}\right) \tag{7}$$

Results using eqns. (1) - (7) are plotted in Fig. 3. The values of several key parameters have been fixed as follows: A_2/A_8 = 1.75, χ_3 = 35°, V_{x3}/V_{x2} = 1.2. These values are based on rough estimates for a typical engine fan system, such as that presented later (Fig. 4(b)). In the case without loss, p_{08}/p_{01} = 1, otherwise eqn. (7) is used with $Y_{P,R}$ = $Y_{P,S}$= 0.15. These values of loss coefficients are broadly based on the values shown later in Fig. 5. They are intended to be representative values for windmill operation, but are not accurate. In the case with deviation, $\delta = 5^\circ$ (i.e. β_3 = 40°) is specified to be typical and to give a significant impact on the fan performance.

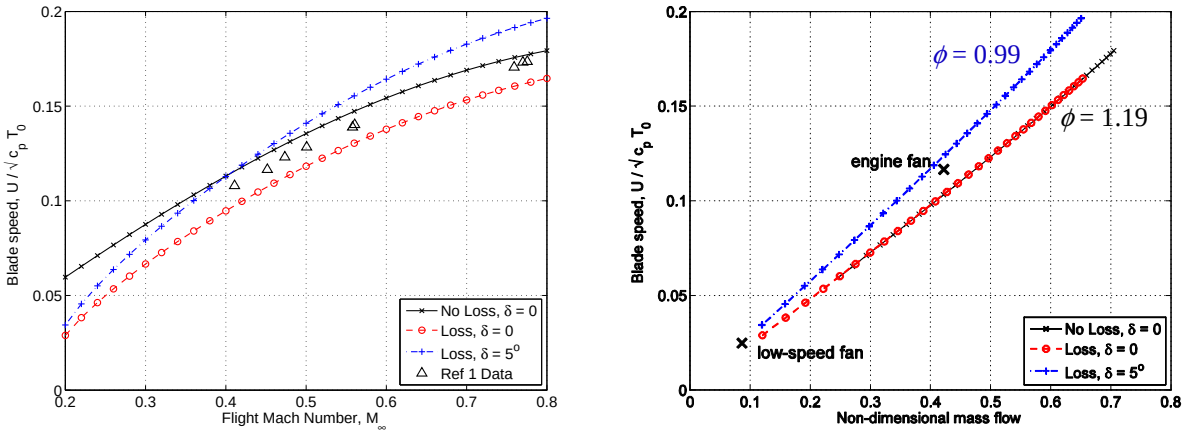

(a) Variation with flight Mach number **(b) Variation with non-dimensional mass flow**

Figure 3: Fan non-dimensional speed at windmill as given by eqns. (1) - (7).

Figure 3(a) shows that as loss is introduced, the non-dimensional mass flow is reduced for a given flight Mach number (eqn. (2)), and thus the blade speed reduces (eqn. (6)). Deviation acts to increase the fan tip speed, since it reduces the fan flow coefficient (eqns. (5) and (6)). Also plotted on Fig. 3 (a) are results derived from Prasad and Lord (2010), which show a similar variation of fan speed with flight Mach number. Figure 3(b) shows the same results but the fan speed is plotted as a function of non-dimensional fan mass flow. Also shown on here are the operating points of the test cases (*low-speed fan* and *engine fan*) investigated in the following sections of this paper, which line up well with the analysis results. Note that for a fixed rotor exit flow angle, the relationship between blade speed and mass flow is linear and independent of loss. This is to be expected from eqn. (6): the exit relative flow angle fixes the windmill flow coefficient and thus the blade speed is linearly proportional to mass flow. This linear relationship was observed in prior work such as Prasad and Lord (2010) and García Rosa et al. (2012). However, the above analysis shows that the variations in windmill speed shown in Fig. 3 are simply a result of the fundamental laws applied to the engine streamtube.

Axial Momentum

Finally, conservation of momentum can be applied. The axial pressure forces on the control volume should balance because the static pressure is equal at inlet and exit. The internal drag force on the streamtube is therefore given by:

$$F_D = \rho_\infty A_\infty V_\infty^2 - \rho_j A_j V_j^2 \tag{8}$$

This can be expressed in terms of non-dimensional parameters as:

$$\Rightarrow \frac{F_D}{p_{01} A_2} = \tilde{m} \frac{V_\infty}{\sqrt{c_p T_{01}}} - Q\left(M_j\right) \frac{V_j}{\sqrt{c_p T_{08}}} \frac{A_N p_{08}}{A_2 p_{01}} \tag{9}$$

As expected, with zero loss eqn. (9) combined with eqns. (2) and (3) gives zero drag. With losses from eqn. (7), for a fan diameter of 3m, a flight altitude of 11 km and M_∞= 0.7, the drag force given by eqn. (9) is 4.0kN. The control volume analysis therefore gives a quick means to estimate the drag on the engine streamtube. However, it should be remembered that a significant amount of drag on a windmilling turbofan will also arise from the spillage flow that passes over the outer nacelle and this is not included here.

In summary, the above analyses show that losses affect the engine mass flow and drag at windmill, whereas the rotor deviation modifies the fan flow coefficient and hence the rotational speed.

TEST CASES AND METHODS

The windmilling performance of two specific fan geometries is now considered. The first is a low-speed, single-stage experimental rig shown in Fig. 4(a) consisting of a spinner, rotor and stator. An unsteady CFD calculation of the windmill test case was also carried out. The second is a representative transonic fan geometry with a modern wide-chord swept rotor, shown in Fig. 4(b), which was tested at windmill using the same CFD methods.

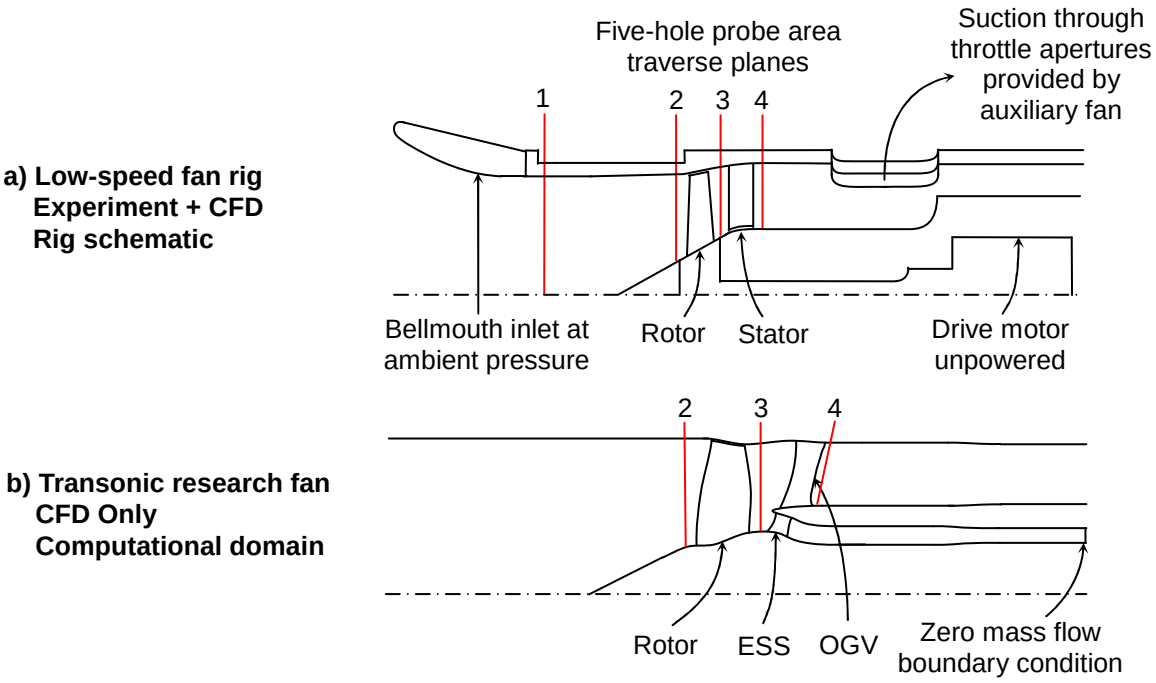

Figure 4: Scale meridional views of the fan rig and the engine fan computational domain.

Experimental Approach

During normal operation at the design point, the rig inlet is at ambient pressure. The rotor is powered directly by a drive motor and the flow exhausts to atmosphere through throttle apertures downstream of the stator blades. For windmilling operation, the throttle apertures were connected through an airtight seal to the inlet of an auxiliary wind tunnel fan. The rig inlet was unmodified compared with the design point and remained at ambient pressure. The auxiliary fan was used to suck air through the rig while the drive motor was left unpowered and the electrical circuit was left open. The fan rotor was then freewheeling at nearly zero net work input, except for a small amount of windage and friction on the drive shaft, providing a true, steady windmilling operating point.

Measurements were performed with a slow-response five-hole pressure probe area traverse at three axial planes, indicated by stations 2, 3 and 4 in Fig. 4(a). The probe measures the time-

averaged stagnation and dynamic pressures and the swirl and radial flow angles. At the design point, the uncertainties in the pressures are 0.1% and 0.5% of dynamic head respectively, and 0.5° in flow angle. At windmill the uncertainties are expected to be greater, particularly at stator exit, because of the presence of large regions of unsteady, separated and intermittently reversed flow.

Ambient pressure and temperature were logged throughout the experiment to calculate the density, which was assumed to be constant because the flow in the rig is incompressible. The 3D velocity field, work and entropy can be derived from the five-hole probe pressure measurements and the density, and these were used to calculate loss breakdowns for comparison with the CFD. The probe moves radially and circumferentially on a grid of points within a 36° sector of the rig, with around 1200 to 2000 measurement points at each station. These measurements were pitchwise-averaged to obtain flow profiles and mass-averaged to calculate overall performance parameters for the stage. Further information on the low-speed rig and measurement techniques are available in Gunn and Hall (2014).

Computational Approach

Unsteady simulations were performed of both the low-speed fan rig at the rig test condition and of the high-speed research fan using Turbostream (Brandvik and Pullan, 2009), a three-dimensional URANS code. The model is second-order accurate in space and time using the dual time-stepping method (Jameson, 1991). The Spalart-Allmaras turbulence model (Spalart and Allmaras, 1994) was used with adaptive wall functions and y_+ values of about 5 on solid boundaries. All simulations were performed as unsteady calculations because the flow field at windmill was known to contain large, unstable regions of separated flow. Neither the model nor the wall functions were designed for highly separated flows, but all turbulence models struggle in such flows and the use of unsteady calculations was found to be the best way to overcome this. 144 timesteps were used per rotor blade passing; higher values did not significantly affect the solutions. The simulations were run for about 10 rotor revolutions. After this point the time-averaged flow field over one rotor revolution was found to be independent of further run-time and the calculation was deemed to have reached a periodic state.

The computational domain consisted of a $1/10^{th}$ sector of the annulus for the low-speed rig (2 rotor and 3 stator passages) and a $1/6^{th}$ sector for the high-speed fan (3 rotor, 7 OGV and 7 ESS passages), with sliding plane interfaces between the blade rows. Grids were generated using Rolls-Royce's PADRAM (Shahpar and Lapworth, 2003) using a structured multiblock HOH topology, with an O-mesh surrounding each blade. Approximately 2 million nodes were used per rotor passage and the total grid sizes for the rig and engine fan were 8 and 17 million nodes respectively. Inlet boundary conditions of uniform axial flow were imposed in both cases, at station 1 for the low-speed rig in Fig. 4(a) and at the inlet to the domain in Fig. 4(b) for the high-speed fan A free stream turbulence intensity of 1% was estimated for both fans and the inlet turbulence length scale was set to about 3% of pitch. Changing these values had little effect on the solutions.

The exit boundary condition for the low-speed rig was a simple back pressure condition applied downstream of the stator. To set the windmilling operating point, the back pressure and shaft speed were matched to the test condition. A preliminary calculation was run and the resulting stage loading value was compared with the measured value. Some minor adjustments to the back pressure and shaft speed were then made to achieve the correct stage loading value.

In the engine fan a similar back pressure boundary condition was imposed in the bypass duct downstream of the OGV. Previous authors have found that at windmill the bypass ratio increases by an order of magnitude or more compared with the design point so very little mass flow enters the core (Walsh and Fletcher, 2008 and Prasad and Lord, 2010). This effect was approximated in the CFD by applying a zero mass flow boundary condition downstream of the ESS. Initial bypass back pressure and shaft speed values were calculated using the control volume analysis detailed in the previous section. The shaft speed was then iterated until zero stage loading was obtained.

OPERATING CONDITION AND LOSS BREAKDOWN

Table 1 compares the design point and windmilling operating conditions for both fans, evaluated at the mid-span radius. In each case windmilling is characterised by a high flow coefficient, as expected from the control volume analysis (Fig. 3(b)). The stage loading values of both fans are close to zero indicating almost no net work input. The rig test measurements revealed a small negative value, indicating a small amount of friction in the freewheeling motor and bearings. The stage reaction decreases from around 0.8 at design to 0.3 at windmill. This indicates that the stator has a stronger effect on performance and contributes to the majority of the stage pressure drop. Also included in Table 1 are the tip relative Mach numbers, which show how the rig fan is incompressible and the transonic fan is fully subsonic at windmill.

Figure 5 shows the loss distributions in both fans in terms of an entropy loss coefficient:

$$\zeta = \frac{T\Delta s}{0.5V^2} \tag{10}$$

where the velocity term is evaluated at the inlet to each component, in the absolute frame for the stator and the relative frame for the rotor. The advantage of an entropy loss coefficient is that it is valid both for rotating and non-rotating components and for zero or non-zero rotor work input. It can therefore be used to compare the design condition with windmill.

	Low-Speed Rig		Engine Fan	
	Design Point	Windmill	Design Point	Windmill
Flow coefficient: ϕ	0.50	1.02	0.65	1.05
Stage loading: ψ	0.47	– 0.047	0.48	0.00
Stage reaction: Λ	0.81	0.37	0.76	0.33
Rotor tip relative Mach number: M	0.13	0.066	1.25	0.34
Rotor tip diameter (m)	0.47		0.87	

Table 1: Operation conditions and geometry for both fan test cases.

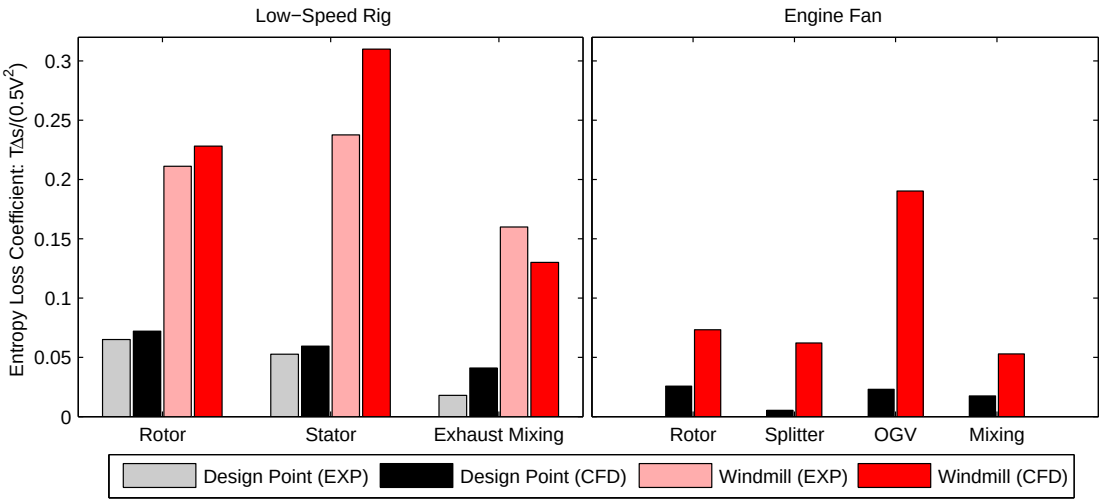

Figure 5: Loss breakdowns at design and windmill.

Comparing experiment with CFD in the low-speed rig, the CFD can be seen to over predict the rotor and stator loss at the design point and at windmill. At the design point, this is attributed to the assumption of fully turbulent boundary layers in the CFD, whereas the rig is expected to have some laminar flow regions in the rotor, and to a slight over prediction in the size of corner separations in

the stator. At windmill, similar arguments apply although the location of laminar flow regions and the form of the corner separations are markedly different.

At windmill, loss increases in every component of both fans compared with the design point. The single greatest loss source in each case is the stator or OGV row, in agreement with the literature. However, in the low-speed rig the rotor also contributes a high amount of loss. In the engine fan, the rotor and splitter combined contribute almost as much loss as the OGV. It is therefore important that none of these loss sources are neglected in models of windmilling fans. In both cases the entropy in the flow field continues to increase downstream of the stator/OGV due to the mixing-out of the highly non-uniform exit flow. This represents a significant additional source of loss which is also increased compared with the design point.

LOW-SPEED FAN AT WINDMILL (TEST & CFD)

Figure 6 shows the flow field through the low-speed fan at windmill. At rotor inlet the flow is swirl-free and the stagnation pressure is uniform apart from the hub and casing boundary layers. The latter is relatively thick due to the low Reynolds number of the rig. The small discrepancy between the experiment and CFD near the hub at rotor inlet is caused by a measurement error due to interference between the probe and spinner geometry. The axial velocity distribution has a similar form to that at the design condition (not shown) but is scaled to a very high flow coefficient as expected from Table 1 and the earlier control volume analysis.

The angular momentum profile in Fig.6 indicates positive rotor work input below 33% span and negative work above. The stagnation pressure profile also passes through zero relative to rotor inlet, but the crossover point is lower down the span because this profile also depends on the loss distribution in the rotor. A large stagnation pressure drop also occurs in the stator, indicating further loss generation. This loss is highest away from the endwalls and is caused by a flow separation from the pressure surface of the blade which is seen in both the experiment and CFD (Fig. 7 (b) and (c)). The CFD contours are taken from a time-averaged solution for a direct comparison with the slow-response five-hole probe measurements. An instantaneous blade-to-blade view of this separation in Fig.8 shows that the separation begins at the leading edge and that the resulting flow field is highly unsteady. The separation creates a blockage which causes the flow to redistribute towards the hub as it passes through the stage, as can be seen in the rotor and stator exit velocity profiles in Fig. 6(b). The redistribution influences the spanwise location where the rotor crosses from positive to negative work. This is because higher axial velocities near the hub raise the power added to the flow by the hub relative to that absorbed by the tip. The rotor and stator performance are therefore coupled.

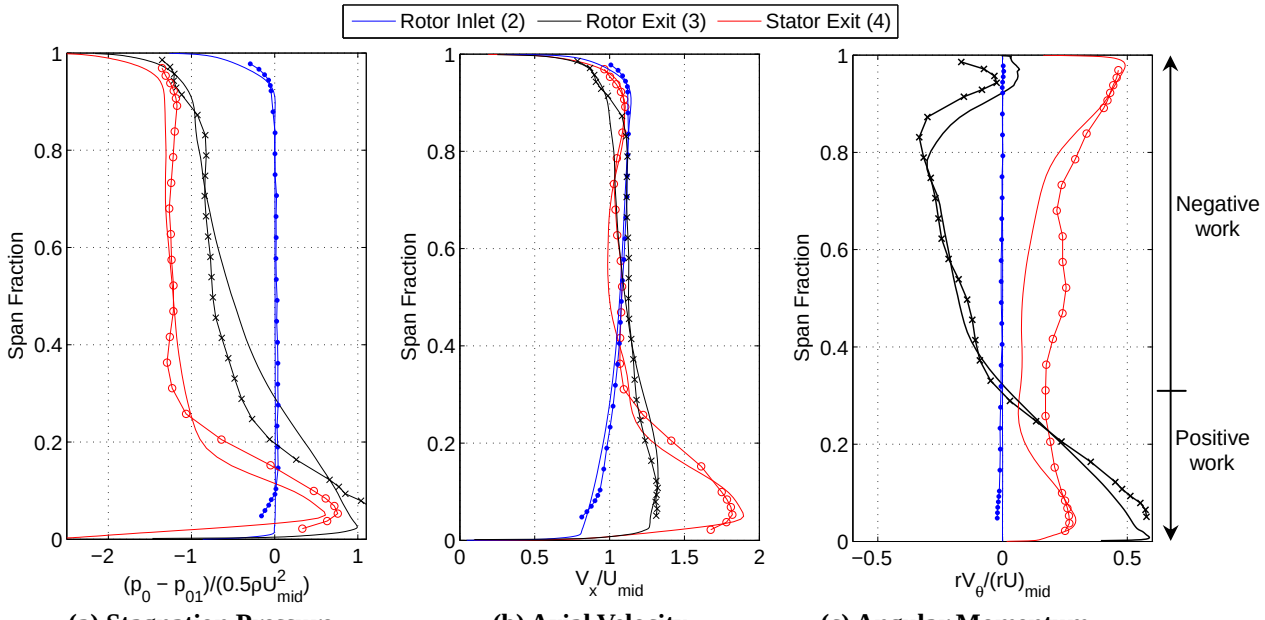

(a) Stagnation Pressure **(b) Axial Velocity** **(c) Angular Momentum**

Figure 6: Spanwise variations in the fan. Experiment: lines with symbols; CFD: solid lines.

The experiment and CFD show similar trends in the radial profiles but the discrepancies are larger than would be expected at the design point. The severely off-design operating point is likely to reduce the accuracy of both experiment and CFD and it is therefore not clear which is most accurate. For example, the Spalart-Allmaras model was not designed for flows with large, unsteady flow separations. This unsteadiness is also not resolved by the five-hole pressure probe. The largest differences are in the stagnation pressure profiles, whereas the axial velocity and work distributions are well matched. This suggests that the flow angles and dynamic head are in broad agreement and therefore that the main difference between the experiment and CFD is in the distribution of loss.

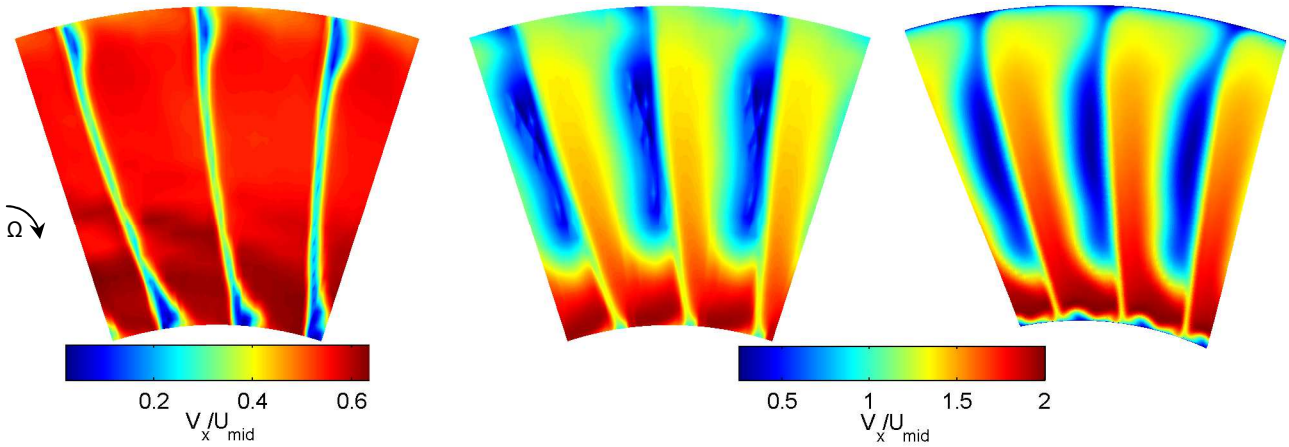

(a) Design point (experiment) **(b) Windmill (experiment)** **(c) Windmill (CFD)**

Figure 7: Stator exit axial velocity contours.

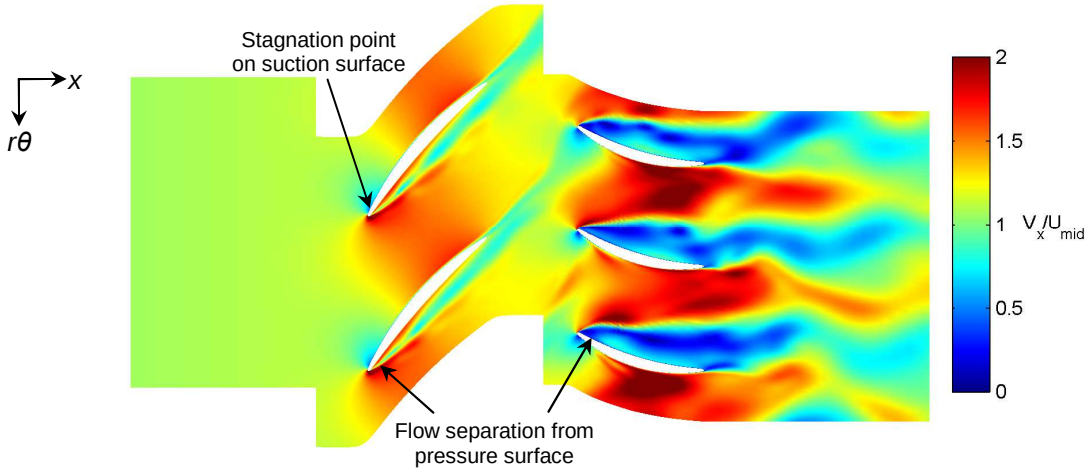

Figure 8: Instantaneous contours of unsteady computed velocity at midspan.

Figure 9(a) shows that the rotor operates at between 10° and 30°of negative incidence relative to the design point. Note that in this figure, angles are positive in the direction of rotor rotation. The incidence leads to a flow separation from the rotor pressure surface, seen in Fig. 8, and causes the observed increase in loss compared with the design condition. The changes in relative flow angle at rotor exit are shown in Fig. 9(b). At both design and windmill conditions there is significant deviation from the exit blade metal angle, which is as expected for a low Reynolds number fan due to the presence of thick boundary layers on the blades. Over most of the span the flow angle is closer to the blade metal angle at windmill than at the design condition, indicating reduced deviation at windmill.

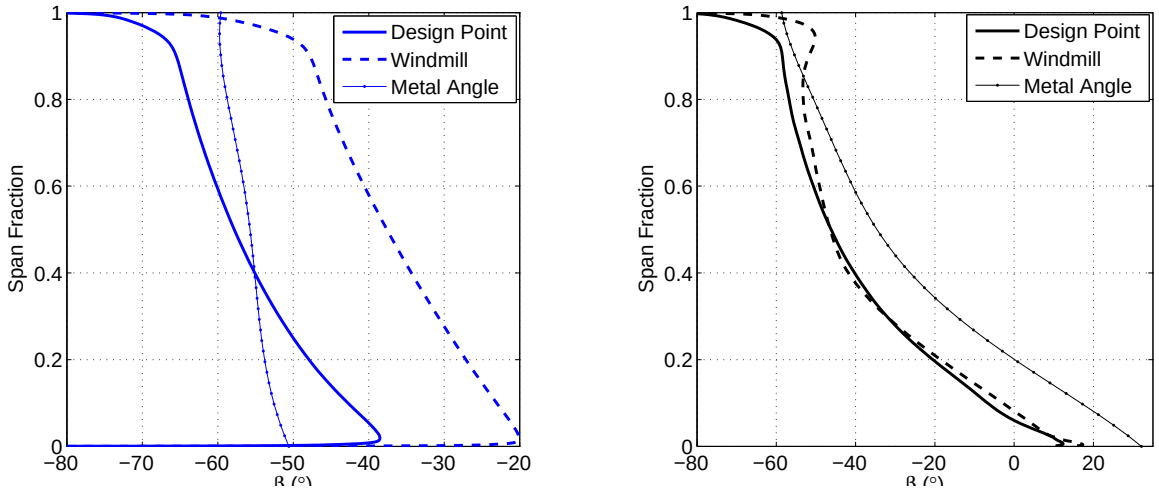

(a) Rotor Inlet **(b) Rotor Exit**

Figure 9: Spanwise variations of inlet and exit rotor relative angles and blade metal angles.

ENGINE FAN AT WINDMILL (CFD)

Radial profiles of axial velocity and angular momentum for the engine fan are shown in Figs. 10(a) and (b). The main difference compared with the low-speed rig is that the blockage distribution downstream of the rotor is different. In this case the core section of the engine fan creates blockage near the hub at rotor exit. This has two related effects. Firstly, the maximum axial velocity at rotor exit now occurs at midspan rather than near the hub and secondly the crossover point between positive and negative work occurs at 60% span. Both of these locations are higher than in the low-speed rig due to the increased hub blockage. In addition the profiles show a region of low axial velocity near the hub at rotor exit. This is caused by a flow separation that is discussed in more detail below.

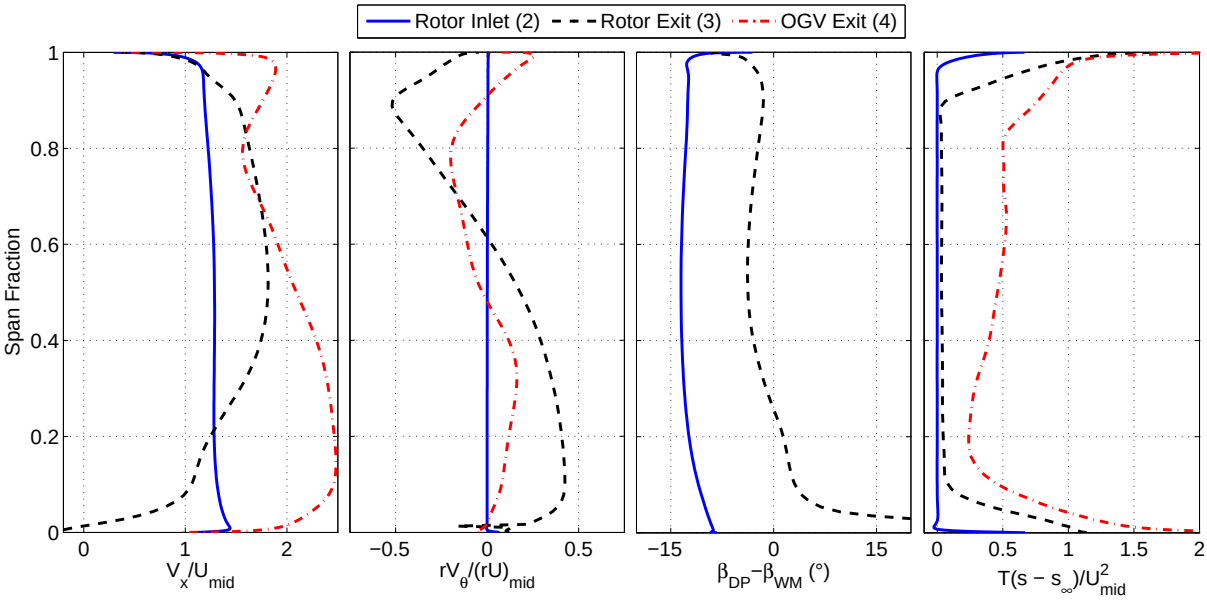

(a) Axial Velocity **(b) Angular Momentum** **(c) Relative Flow Angles** **(d) Entropy**

Figure 10: Spanwise variations in the engine fan at windmill.

The velocity profile at OGV exit is similar to that in the low-speed rig stator, with maximum velocity near the hub. Figure 11(c) shows this is caused by a similar pattern of flow separations in the passages. However because the OGV is situated farther from the rotor in the engine fan, this flow field has less impact on the rotor than the core/splitter blockage.

Figure 10(c) compares the rotor relative flow angles at windmill with the design point. The change in relative inlet flow angle compared with the design condition is smaller than for the low-speed fan. This is because the increase in flow coefficient from the design point to the windmill condition is less for the engine fan than it is for the low-speed fan (see Table 1). Nevertheless, the rotor operates at negative incidence values of over 10°. Similarly to the low-speed rig, the changes in relative exit angle from the design condition are small, but non-zero, over most of the span. As indicated by the earlier control volume analysis, this variation should be taken into account for more accurate windmill performance modeling.

The radial profiles of entropy in Fig. 10(d) reveal the main sources of loss in the stage. At rotor inlet the entropy is almost uniform apart from a small region of high entropy in the casing boundary layer and an even smaller region in the spinner boundary layer. The profile at rotor exit is also uniform away from the endwalls and over most of the span the entropy increase through the rotor is small. Most of the loss is contained in two distinct regions above and below 90% and 10% span respectively. In contrast, the OGV generates high levels of loss all the way up the span through the same pressure surface flow separation seen in the low-speed rig. The loss generated in the stator separation is relatively well understood and discussed extensively in the literature, but Fig. 5 showed that the contributions from the rotor and splitter are also important and these are less well understood. They are therefore discussed in more detail below.

The entropy contours in Fig. 11(a) show that entropy is generated almost axisymmetrically around the hub, but with a slightly higher concentration on the blade suction surfaces. The blade surface streamlines in Fig. 12(a) show the presence of a TE corner separation. This is caused by the blockage effect of the core section just downstream, which causes the flow to redistribute up the span just downstream of the TE. The redistribution also thickens the hub surface boundary layer all around the circumference. A three-dimensional view of this redistribution can also be seen in Fig. 12(c).The streamlines and contours of axial shear stress show that the flow separates from the rotor hub just upstream of the core and remains unattached around the splitter, only reattaching inside the OGV passages. This generates the splitter component of loss shown earlier in Fig. 5.

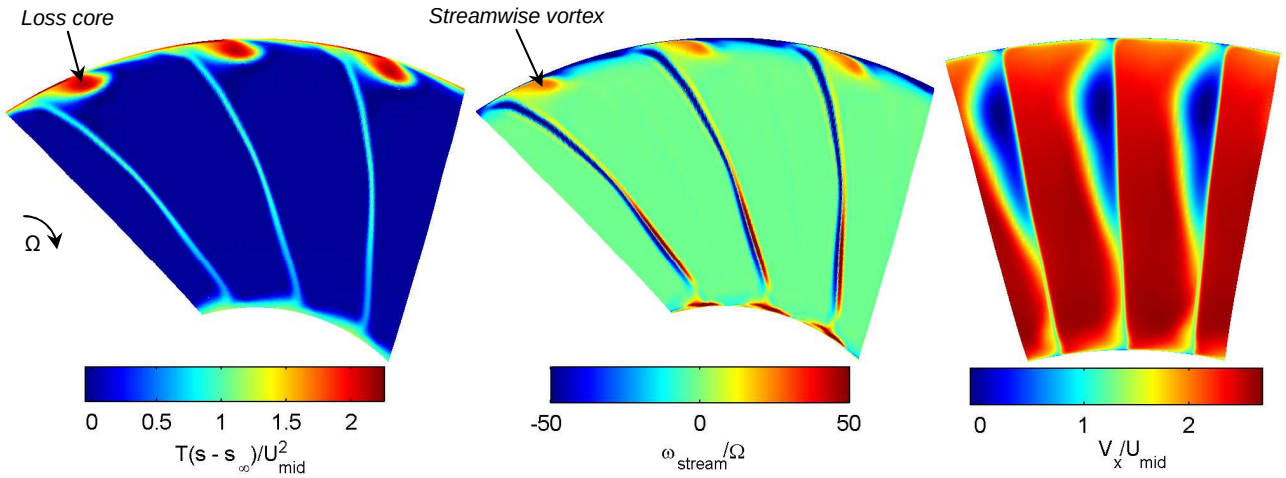

(a) Entropy (Rotor Exit) **(b) Streamwise Vorticity (Rotor Exit)(c) Axial Velocity (OGV Exit)**

Figure 11: Contours of entropy and streamwise vorticity at rotor exit (station 3); and axial velocity at OGV exit (station 4) in the engine fan at windmill.

At the casing, the entropy contours reveal the presence of a loss core close to the pressure surface. A similar feature was observed by Prasad & Lord (2010). In Fig.11(b) a streamwise vortex core can be seen in the same region. Figure12(b) shows that the flow separates at the leading edge on the pressure surface above midspan. This creates a region of reversed flow which is visible in the streamlines. Along the boundary of this region, the flow moves radially up the span and streamwise vorticity is shed into the flow from the blade surface (Figs. 12(b) and (c)). The fluid travelling along this separation line then forms a streamwise vortex near the casing. Comparison with Figs. 11(a)

and (b) shows that the entropy generated in the LE separation is captured by this vortex core, which also captures the tip leakage flow and entrains fluid from the main stream. This explains why the rotor exit entropy profile is low away from the endwalls despite the presence of an LE separation over the entire upper half of the blade.

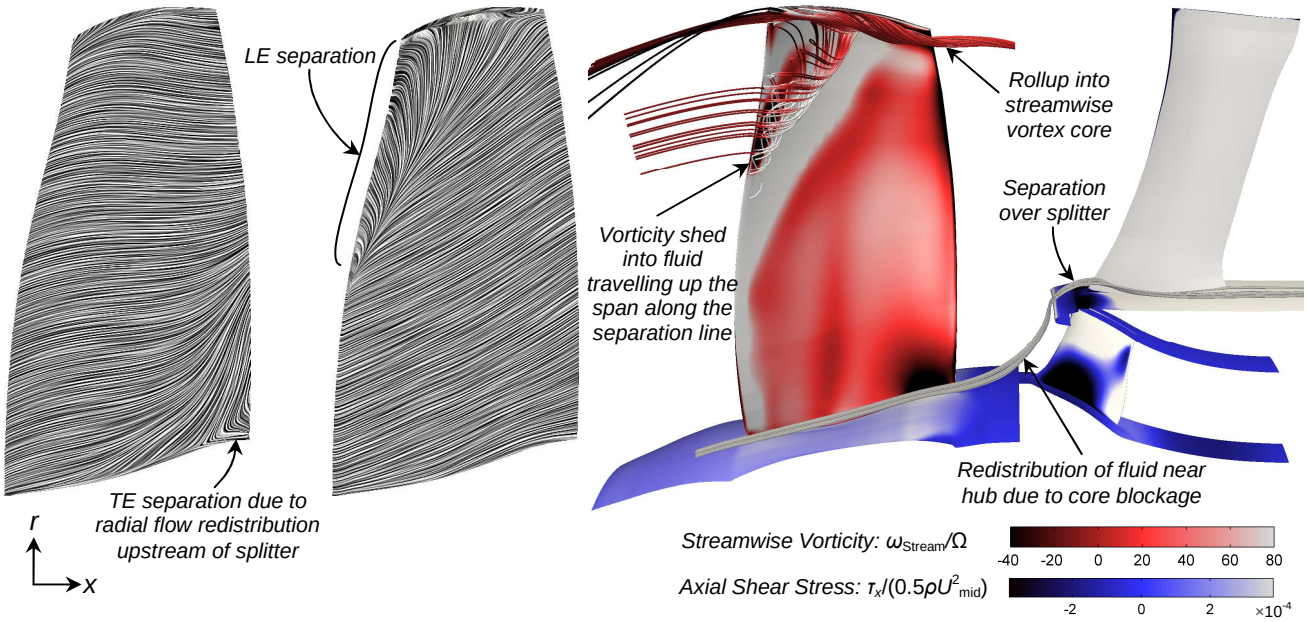

(a) Suction surface flow **(b) Pressure surface flow** **(c) 3D rotor streamlines (view of pressure surface)**

Figure 12: Computed flow visualisations in the engine fan rotor.

In summary, the main loss mechanisms in the engine fan have been shown to be: (i) the combination of an LE separation and streamwise vortex near the rotor casing, (ii) flow separations at the rotor hub and splitter due to redistribution around the engine core and (iii) flow separation from the OGV pressure surface due to negative incidence. In addition, the low-speed rig test showed that computations of windmilling fan performance can provide good estimates of the magnitudes of the loss and of the physical flow features.

CONCLUSIONS

Windmill operation is characterised by a high flow coefficient. This causes the rotor and stator to operate at negative incidence, leading to high loss. The total loss determines the engine drag and affects the engine mass flow, whereas the rotor deviation affects the fan work distribution. Increasing deviation means the rotor acts more like a turbine leading to a higher rotational speed. It is therefore important to know the spanwise variation of rotor relative exit angle with reasonable accuracy.

The rotor performance is influenced by any downstream blockage (e.g. the stator separation in the fan rig or the core and splitter in an engine fan). This alters the radial distribution of mass flow and hence modifies the rotor work distribution. In both the engine and rig fans the rotor deviation is different from that at the design point and tends to increase towards the hub, where the sections are putting work in to the flow and are at high negative incidence.

In both the rig fan and the engine fan, the largest single loss source is the OGV, in agreement with the literature. However, the combined rotor, splitter and mixing losses are just as important. The main rotor loss source is from a leading edge pressure surface separation caused by negative incidence at the windmill condition. In an engine fan this is confined to the tip region and a streamwise vortex forms which contains the entropy from the separation. There is also a rotor hub separation due to the blockage effects of the downstream core section. The main loss source in the stator is the pressure surface separation. There is also additional loss in an engine fan from the separation of the flow over the core section splitter.

ACKNOWLEDGMENTS

The authors would like to thank Adam Bagnall, Ross Maxwell and Chris Sheaf at Rolls-Royce plc. for their technical advice and suggestions. Colin Bullman provided excellent technician support for the low speed rig experiments. Relevant discussions with colleagues Chris Freeman, Dr Tom Hynes, Dr Ivor Day, Dr John Longley and Prof. Nick Cumpsty are also gratefully acknowledged.

NOMENCLATURE

Symbols

A	Area
F	Force
h	Enthalpy
$\dot{m}$	Mass flow rate
M	Mach number
p	Pressure
Q	Non-dimensional mass flow rate
r	Radial coordinate
s	Entropy
T	Temperature
U	Rotor blade speed
V	Velocity
W	Relative velocity
W_x	Shaft power
x	Axial coordinate
Y_P	Stagnation pressure loss coefficient
α	Absolute whirl flow angle
β	Relative flow angle
χ	Blade metal angle
δ	Deviation
ρ	Density
τ	Shear stress
ζ	Entropy loss coefficient
Ω	Shaft angular velocity

Non-Dimensional Groups

ϕ	Flow coefficient: $(\dot{m}/\rho_2 A_2 U) = V_{x2}/U$
ψ	Stage loading coefficient: $(h_{04}-h_{02})/U^2$
Λ	Stage reaction: $(h_3-h_2)/(h_4-h_2)$

Abbreviations

ESS	Engine Section Stator
LE	Leading Edge
OGV	Outlet Guide Vane
TE	Trailing Edge

Subscripts

0	Stagnation quantity
1	Value upstream of spinner
2	Value at rotor inlet
3	Value at rotor exit
4	Value at stator exit
8	Value at nozzle exit
j	Value in exhaust jet
mid	Value at mid-span
rel	Relative frame quantity
R	Rotor
S	Stator
x	Axial component
∞	Far upstream value
θ	Circumferential component

REFERENCES

[1] Prasad, D. and Lord, W.K., 2010, “Internal losses and flow behaviour of a turbofan stage at windmill,” *Journal of Turbomachinery,* 132(3):031007-1-10.

[2] Walsh, P.P., and Fletcher, P., "Windmilling", Gas Turbine Performance, Blackwell Science, Oxford, England, UK, 1998, pp. 501-518.

[3] Mishra, R. K., Gouda, G., and Vedaprakash, B. S. (2008). "Relight Envelope of a Military Gas Turbine Engine: An Experimental Study.", ASME Conference Proceedings , 2008(43116):55–60

[4] García Rosa, N., Pilet, J., Lecordix, J-L., Barènes, R., Lavergne, G., (2013), "Experimental analysis of the flow through the fan stage of a high-bypass turbofan in windmilling conditions", ETC Conference Procedings.

[5] Braig, W., Schulte, H., and Riegler, C. (1999). "Comparative analysis of the windmilling performance of turbojet and turbofan engines.", *Journal of Propulsion and Power* , 15(2):326–333.

[6] Goto, T., Kato, D., Ohta, Y., Outa, E., (2014) "Unsteady flow structure in an axial compressor at windmill condition", ASME Turbo Expo, GT2014-25609.

[7] Courty-Audren, S., Binder, N., Carbonneau, X., Challas, F., (2010) "Potential of power recovery of an axial fan in windmilling operation", ETC Conference Procedings.

[8] A. Gill, T. W. von Backstrom, T. M. Harms, (2010) "The flow field within an axial flow compressor at extremely high flow coefficients", ASME Turbo Expo, GT2010-22894.

[9] Cumpsty, N.A., and Heyes, A., Jet Propulsion, 3rd Edition, Cambridge University Press, England, UK, 2015, pp. 99-113.

[10] E. J. Gunn and C. A. Hall, (2014) "Aerodynamics of boundary layer ingesting fans", ASME Turbo Expo, June 16-20, 2014, Düsseldorf, Germany, GT2014-26142.

[11] Brandvik, T. and Pullan, G., (2011) “An Accelerated 3D Navier-Stokes Solver for Flows in Turbomachines”, *Journal of Turbomachinery*, 133(2):021025.

[12] Shahpar, S. and Lapworth, L. (2003), “PADRAM: Parametric Design and Rapid Meshing System for Turbomachinery Optimisation,” Proceedings of ASME Turbo Expo 2003, GT2003-38698.

[13] Spalart, P. R. and Allmaras, S. R. (1994), “A One-Equation Turbulence Model for Aerodynamic Flows”, *La Recherche Aérospatiale*, 1:5-21.

[14] Jameson, A. (1991), “Time Dependent Calculations Using Multigrid, with Applications to Unsteady Flows Past Airfoils and Wings,” Proceedings of AIAA 10th Computational Fluid Dynamics Conference, AIAA 91-1596.

Figure Captions List

Fig. 1 Velocity triangles for a windmilling fan section

Fig. 2 Capture streamtube used as the control volume for a windmilling turbofan

Fig. 3 Fan non-dimensional speed at windmill as given by eqns. (1) - (7)

Fig. 4 Scale meridional views of the fan rig and the engine fan computational domain

Fig. 5 Loss breakdowns at design and windmill

Fig. 6 Spanwise variations in the fan. Experiment: lines with symbols; CFD: solid lines.

Fig. 7 Stator exit axial velocity contours

Fig. 8 Instantaneous contours of unsteady computed velocity at midspan

Fig. 9 Spanwise variations of inlet and exit rotor relative angles and blade metal angles

Fig. 10 Spanwise variations in the engine fan at windmill

Fig. 11 Contours of entropy and streamwise vorticity at rotor exit (station 3); and axial velocity at OGV exit (station 4) in the engine fan at windmill.

Fig. 12 Computed flow visualisations in the engine fan rotor

Table Caption List

Table 1 Operation conditions and geometry for both fan test cases

